RESEARCH ARTICLE SUMMARY

DEVELOPMENTAL BIOLOGY

Contact area–dependent cell communication and the morphological invariance of ascidian embryogenesis

Léo Guignard*, Ulla-Maj Fiúza*, Bruno Leggio, Julien Laussu, Emmanuel Faure, Gaël Michelin, Kilian Biasuz, Lars Hufnagel†, Grégoire Malandain†‡, Christophe Godin†‡, Patrick Lemaire†‡

INTRODUCTION: Within each animal species, embryonic development is highly reproducible, ensuring the faithful production of a complex organism with precisely arranged and shaped organs. In most animal embryos, reproducibility is found at the tissue scale, the behaviors of individual cells being stochastic beyond the first cell divisions. Ascidians, a group of marine invertebrate chordates, show an extreme form of embryonic reproducibility: Homologous cells can be found across individual embryos, and early embryonic cell lineages are considered invariant. Embryonic geometries are even conserved between species, which diverged 400 million years ago and have very dissimilar genomes. Because of their evolutionary conservation of early embryonic development and ability to buffer genetic divergence, ascidians constitute attractive model systems to study the mechanisms driving cellular reproducibility.

RATIONALE: To quantify embryonic reproducibility in the ascidian *Phallusia mammillata*, we first built a high-resolution atlas of embryonic cell lineages, cell shapes, and cell interactions. We imaged 10 live embryos every 2 min up to the end of the neurula stages using multiview light-sheet microscopy. To systematically measure the developmental variability of a range of temporal and spatial cellular features, we developed a robust and scalable adaptive segmentation and tracking of embryonic cells procedure (ASTEC) compatible with high-throughput multiview light-sheet imaging datasets. We related these features to cell fate specification, which in ascidians is mainly controlled by differential sister cell inductions. Inspired by previous work indicating that the area of contact to signaling cells controls ascidian neural induction, we integrated our geometric description with a signaling gene expression atlas. This integration allowed us to test, through computational and experimental approaches, the hypothesis that contact area–dependent cell communication imposes constraints on embryonic geometries.

RESULTS: We found that, up to the neurula stages, *Phallusia* embryos develop without cell growth, programmed cell death, or cell neighbor exchanges. Beyond cell position, cell cycle duration, and cell lineages, we observed a high reproducibility of cell arrangements: 75% of cells shared at least 80% of their neighbors in all 10 embryos studied. Furthermore, the areas of contact between homologous cells varied by less than 20% across embryos. Mechanistically, we uncovered a tight link between the control of cell arrangements and asymmetric cell divisions, which give rise to sister cells of distinct fates. We then combined computational and experimental approaches to reveal that areas of cell contact between signaling and responding cells have sufficient encoding potential to explain all known early embryonic inductions, without the need to invoke gradients of ligand concentration. Finally, using geometrical perturbations of embryonic development we demonstrated that precise areas of cell-cell contact were important for mesendodermal and neural fate specification.

ON OUR WEBSITE

Read the full article at https://dx.doi.org/10.1126/science.aar5663

CONCLUSION: Our work establishes the highly reproducible ascidian embryo as a framework to bridge cell behaviors, morphogenesis, and the underlying regulatory program. The ASTEC pipeline allows systematic automated whole-cell segmentation and tracking across whole embryos in high-throughput light-sheet datasets. Second, we establish the geometric control of embryonic inductions as an alternative to classical morphogen gradients and suggest that the range of cell signaling events sets the scale at which embryonic reproducibility is observed. Finally, our study suggests that the high level of reproducibility of ascidian embryonic geometries may paradoxically lift constraints on the evolution of ascidian genomes, thereby contributing to rapid molecular evolution. ■

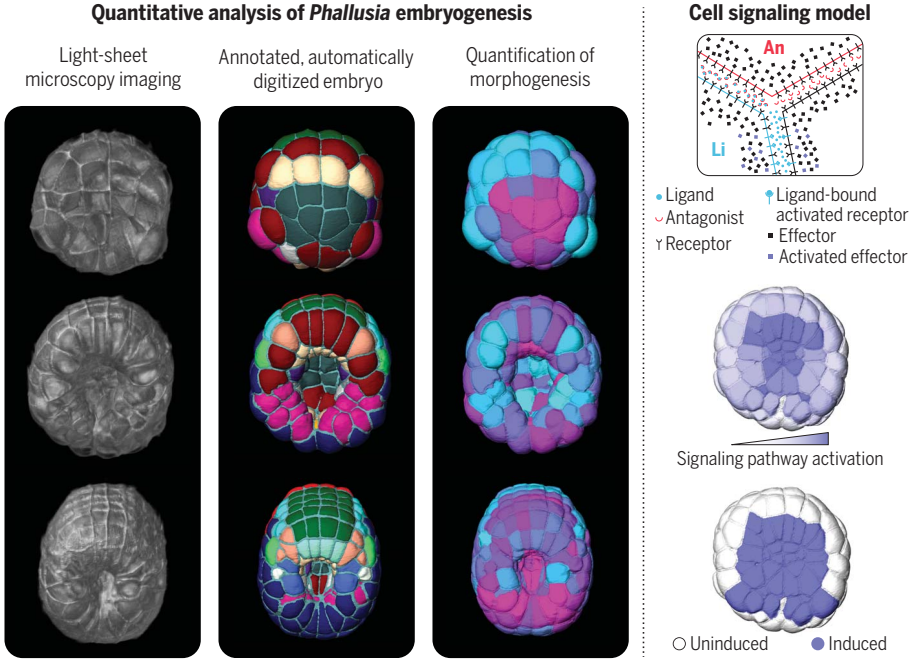

Reconstruction and modeling of *Phallusia* embryogenesis. (Left) Quantitative analysis of *Phallusia* embryogenesis. We combined live light-sheet imaging of cell membranes (left images) with automated cell segmentation and tracking with color-coded cell fates (center images) to extract quantitative cell morphological properties (right images, color-coded by cell compactness). From top to bottom: embryo at the 64-cell, mid-gastrula, and late gastrula stages. (Right) Cell signaling model. We first made simplifying assumptions concerning the distribution and diffusion of signaling pathway components (top) and then integrated cell contact geometry with gene expression profiles to predict pathway activation levels in single cells (center) and binarized induction status (bottom).

The list of author affiliations is available in the full article online.
*These authors contributed equally to this work.
†Corresponding author. Email: hufnagel@embl.de (L.H.); gregoire.malandain@inria.fr (G.Ma.); christophe.godin@inria.fr (C.G.); patrick.lemaire@crbm.cnrs.fr (P.L.)
‡These authors contributed equally to this work.
Cite this article as L. Guignard *et al.*, *Science* **369**, eaar5663 (2020). DOI: 10.1126/science.aar5663

RESEARCH ARTICLE

DEVELOPMENTAL BIOLOGY

Contact area–dependent cell communication and the morphological invariance of ascidian embryogenesis

Léo Guignard[1,2,3]*†, Ulla-Maj Fiúza[1,4]*, Bruno Leggio[1,2,5], Julien Laussu[1]‡, Emmanuel Faure[1,2,6]§, Gaël Michelin[7], Kilian Biasuz[1], Lars Hufnagel[4]¶, Grégoire Malandain[7]¶#, Christophe Godin[2,5]¶#, Patrick Lemaire[1]¶#

Marine invertebrate ascidians display embryonic reproducibility: Their early embryonic cell lineages are considered invariant and are conserved between distantly related species, despite rapid genomic divergence. Here, we address the drivers of this reproducibility. We used light-sheet imaging and automated cell segmentation and tracking procedures to systematically quantify the behavior of individual cells every 2 minutes during *Phallusia mammillata* embryogenesis. Interindividual reproducibility was observed down to the area of individual cell contacts. We found tight links between the reproducibility of embryonic geometries and asymmetric cell divisions, controlled by differential sister cell inductions. We combined modeling and experimental manipulations to show that the area of contact between signaling and responding cells is a key determinant of cell communication. Our work establishes the geometric control of embryonic inductions as an alternative to classical morphogen gradients and suggests that the range of cell signaling sets the scale at which embryonic reproducibility is observed.

The development of each animal species is highly reproducible, ensuring the faithful replication of a complex organism in which organs are precisely shaped, sized, and positioned. This fidelity of embryogenesis despite genetic polymorphism and fluctuating environmental conditions is critical for the perpetuation of species.

Reproducibility can be observed at different scales. Many vertebrate and invertebrate embryos initially display a stereotyped pattern of orientation and geometry of individual cell divisions, which can be explained by simple self-organizing mechanical rules (*1*). This initial cellular reproducibility is usually lost during early cleavage stages, as the number of cells increases. It is, however, maintained during later developmental stages in nematodes (*2*) and in ascidians (*3*), a group of marine invertebrates closely related to vertebrates (*4*). Unlike those of nematodes (*5*), ascidian embryo geometries have even remained essentially unchanged since the emergence of the group, around 400 million years ago (*3*, *6*), despite extensive genomic divergence and gene regulatory network rewiring (*7*). Because of the distinctive evolutionary conservation of their early embryonic development and because of their notable ability to buffer genetic divergence, ascidians constitute an attractive model system to study the mechanisms driving and maintaining cellular reproducibility.

Development of ascidians and nematodes is characterized by lower cell number and earlier fate restriction than most animal embryos. Ninety four of the 110 early gastrula cells in the ascidian *Halocynthia roretzi* are fate restricted, each contributing to a single larval tissue type (*8*). Most mesendodermal tissues are generated by a very small, and specific, number of fate-restricted early gastrula progenitors: six for the notochord, four for the mesenchyme, and two for the heart or trunk lateral cells (*8*). Although reduced cellular complexity alone cannot explain invariance (*9*), the precision of the mechanisms needed to specify a small, specific number of fate-restricted progenitors of each tissue may impose constraints favoring developmental invariance.

Short-range cell communication plays a crucial role in the specification of most of the ascidian mesendodermal and neural lineages (*10*, *11*). Previous work on the induction at the 32-cell stage of ascidian neural progenitors by fibroblast growth factor (FGF) revealed that this induction only occurs in the four ectodermal cells whose area of contact to FGF-emitting cells exceeds a threshold value (*12*). This contact area–dependent induction exemplifies how the specification of a precise number of tissue precursors can rely on the precise spatial arrangement of individual embryonic cells.

In this work, we tested the hypothesis that complex feedback between fate specification and morphogenetic processes, whose strength is amplified by the reduced cell number, promotes developmental invariance. We first developed methods to quantitatively study cellular variability in the ascidian *Phallusia mammillata*. We then used these methods in the chordate embryo to explore the relationships between

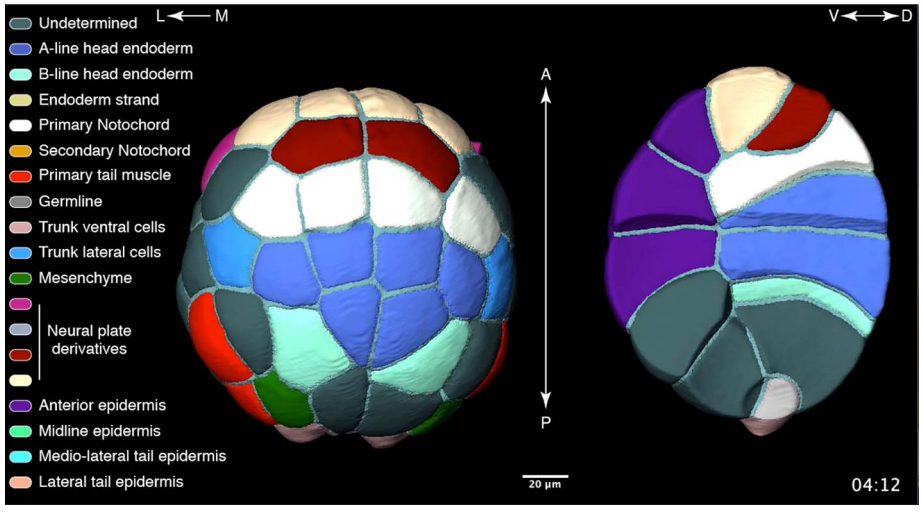

Movie 1. Digitized *P. mammillata* embryo. Vegetal view (left) and side view through a sagittal section (right) of the ASTEC-Pm1 segmented and fate-colored *P. mammillata* embryo. Anterior is to the top. The tissue fate color code is shown on the left-hand side.

[1]CRBM, Université de Montpellier, CNRS, 34293 Montpellier, France. [2]Virtual Plants, Université de Montpellier, CIRAD, INRA, Inria, 34095 Montpellier, France. [3]Janelia Research Campus, Howard Hughes Medical Institute, Ashburn, VA 20147, USA. [4]Cell Biology and Biophysics Unit, European Molecular Biology Laboratory, 69117 Heidelberg, Germany. [5]Laboratoire Reproduction et Développement des Plantes, Université de Lyon, ENS de Lyon, UCB Lyon 1, CNRS, INRA, Inria, 69342 Lyon, France. [6]Institut de Recherche en Informatique de Toulouse (IRIT), Universités Toulouse I et III, CNRS, INPT, ENSEEIHT, 31071 Toulouse, France. [7]Morpheme, Université Côte d'Azur, Inria, CNRS, I3S, France.
*These authors contributed equally to this work.
†Present address: Max Delbrück Center for Molecular Medicine in the Helmotz Association, Berlin Institute of Health, 10115 Berlin, Germany. ‡Present address: Institut Clément Ader, Université Toulouse III, CNRS, INSA, ISAE-SUPAERO, Mines-Albi, 31400 Toulouse, France. §Present address: Equipe ICAR, LIRMM, Université de Montpellier, CNRS, 34095 Montpellier, France.
¶Corresponding author. Email: hufnagel@embl.de (L.H.); gregoire.malandain@inria.fr (G.Ma.); christophe.godin@inria.fr (C.G.); patrick.lemaire@crbm.cnrs.fr (P.L.) #These authors contributed equally to this work.

the reproducibility of cell arrangements, the precision of fate specification processes, and the range of embryonic inductions.

A high-resolution geometric atlas of embryonic cell shapes and interactions

Using confocal multiview light-sheet microscopy (*13*), we imaged the development of 10 optically transparent *P. mammillata* embryos with fluorescently labeled plasma membranes, every 2 min from cleavage to neurula stages (Fig. 1A, figs. S1 to S4, table S1, and movies S1 and S2). Systematic segmentation and long-term tracking of all membrane-labeled cells of a developing embryo remain challenging (*14*), despite recent advances (*15*–*19*). Analysis of the limitations of our previous two-pass multiangle image acquisition, three-dimensional reconstruction and cell segmentation–automated lineage tracking (MARS-ALT) pipeline (*20*) (figs. S5 to S8) guided the development of an algorithm adapted to high-throughput light-sheet datasets called ASTEC, for adaptive segmentation and tracking of embryonic cells (Fig. 1, B and C). ASTEC is a single-pass algorithm that simultaneously segments and tracks whole cells by iteratively projecting segmentations from one time point onto the next (figs. S9 to S14). ASTEC produces a digitized version of each embryo: a segmentation of all embryonic cells existing at each time point, integrated into global cell lineages, to which we associated their known larval tissue fates and from which quantitative geometrical parameters can be extracted (Fig. 1D, figs. S15 to S17, Movie 1, and movie S3). The 10 digitized *P. mammillata* embryos, ASTEC-Pm1 to ASTEC-Pm10, constitute a quantitative and dynamic atlas of cell positions, geometries, and ancestry over a large fraction of a metazoan developmental program (Movie 2 and movie S4), which can be interactively explored through the MorphoNet online morphological browser (*21*).

Figure 1C illustrates the ASTEC-Pm1 digitized embryo, which contains a total of 67,003 segmented three-dimensional (3D) cell "snapshots," and describes the behavior over time of 1395 individual cells generated by 697 cell division events. Manual inspection revealed that the pipeline only missed 4/1399 cells and 3/700 cell divisions, and it assigned 99% of voxels to the correct cell (figs. S6 and S18 and tables S2 and S3). In a manner consistent with previous work in another ascidian species (*22*), no programmed cell death was detected, such that all cells but one were tracked until their division or the end of the movie (fig. S15). On this dataset, ASTEC outperformed RACE, a reference membrane–based segmentation algorithm adapted to embryonic datasets (*16*) (fig. S19). The segmentation and tracking accuracy of all 10 embryos was comparable to that of ASTEC-Pm1 (tables S2 and S3).

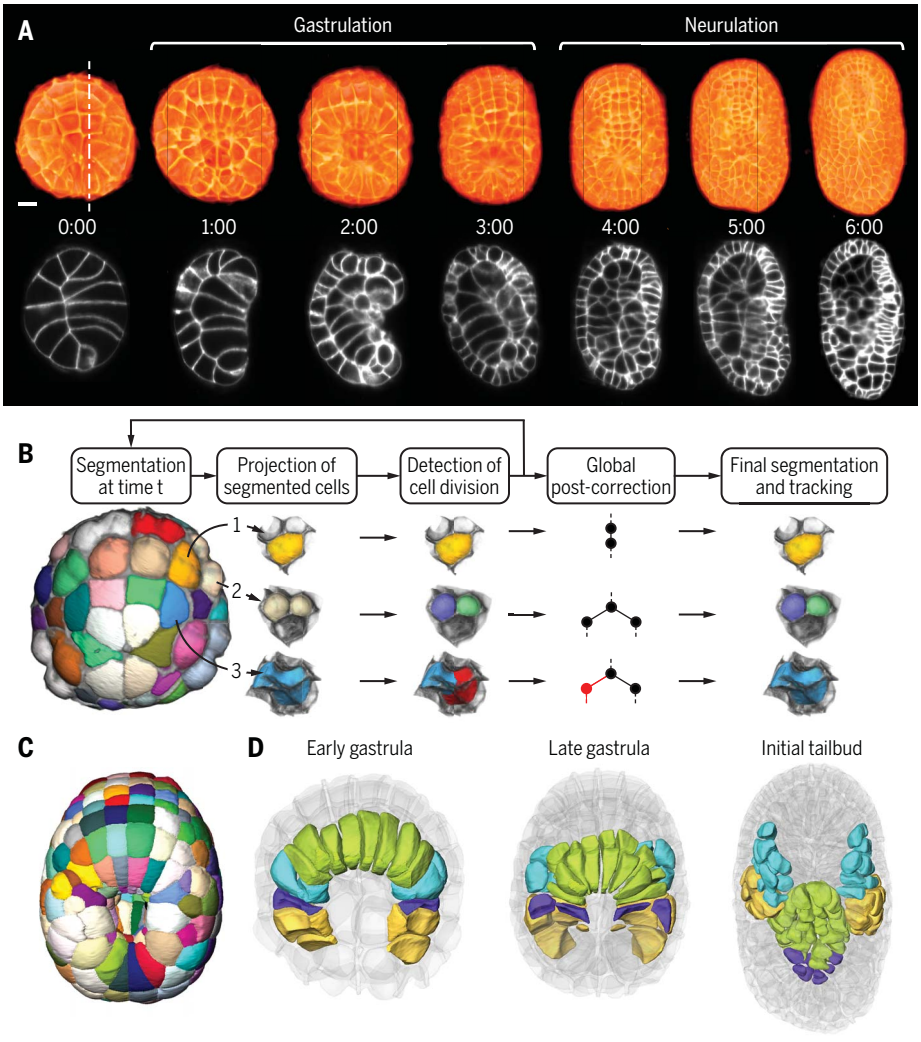

Fig. 1. High-resolution multiview light-sheet imaging and segmentation of *P. mammillata* embryos. (**A**) (Top) Vegetal and dorsal views of 3D rendering at the indicated time points of the imaged embryo after fusion of the images taken along the four angles of view. The time scale indicates the duration of imaging in hours. (Bottom) Parasagittal sections along the plane shown with the vertical dashed white line. Scale bar, 20 μm. (**B**) The ASTEC pipeline. Different cases are illustrated: a nondividing cell (yellow), a dividing cell (white), an oversegmented nondividing cell (blue) corrected during postcorrection. For more details, see fig. S9. (**C**) Dorsal view of the segmentation of ASTEC-Pm1 at the late gastrula stage (time t = 2 hours 30 min). Colors are arbitrary. (**D**) Position of mesoderm progenitors in ASTEC-Pm1 at the early gastrula (t = 1 hour 10 min), late gastrula (t = 2 hours 40 min), and late neurula (t = 4 hours 40 min) stages. B-line mesenchyme, yellow; trunk lateral cells, cyan; primary notochord, green; secondary notochord, purple. Anterior is to the top. For more details, see fig. S16.

Ascidian development is reproducible down to the scale of cell-cell contacts

We systematically measured the developmental variability of a range of temporal and spatial cell features during gastrulation and neurulation. At the temporal level, the median variability of the cell cycle durations of homologous cells (equivalent bilateral cells within an embryo or across embryos) was on the order of one time point, within the image sampling error (figs. S20 to S22). The cell lineages of homologous cells were similar (Fig. 2A), as quantified with a normalized tree-edit distance capturing the average cost per cell of the transformation of one tree into the other (fig. S23). This high lineage similarity led to a quasi-invariant number of cells at any given developmental stage across the 10 embryos (2% average variation in cell number across all embryos) (Fig. 2B). At the spatial level, we observed up to a twofold variation in the total volume of individual embryos, reflecting egg size heterogeneity, as no cell growth occurred during the considered developmental period (fig. S24). The relative cell volumes (i.e., cell volume divided by total embryo volume) (fig. S25) and relative cell

positions of matching cells within and between embryos (Fig. 2, C and D) had, however, a median variability below 5%, highlighting the reproducibility of cell geometries and positions as well as their scaling with egg size. The reproducibility of relative cell positions was higher in *Phallusia* than in a *Caenorhabditis elegans* dataset (*23*) (Fig. 2C and fig. S26). Cell neighborhoods were also highly conserved: Up to the late neurula stage, 75% of matching cells shared at least 80% of their physical neighbors across all embryos (Fig. 2D and fig. S27). Most shared cell contacts lasted throughout the cell cycle (fig. S27), such that cell neighbor exchanges, a major source of stochastic variability during animal embryogenesis, were rare. The relative areas of shared cell-cell contacts varied by less than 20% across the 10 embryos (Fig. 2E).

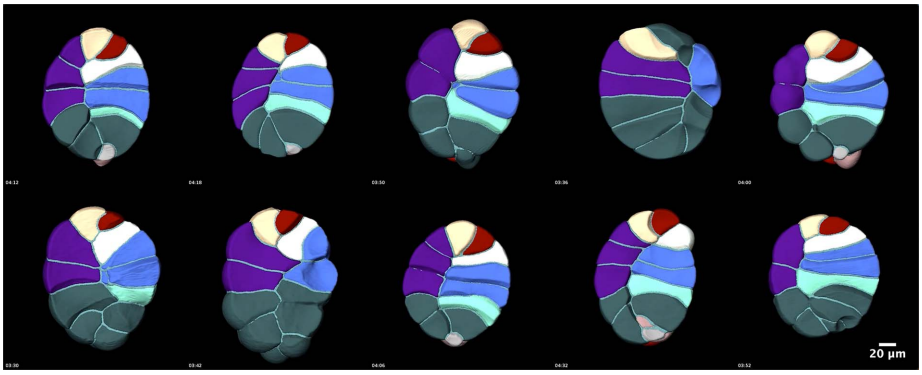

Movie 2. Sagittal section of 10 digitized *P. mammillata* embryos. Side views through sagittal sections across the ASTEC-Pm1 to ASTEC-Pm10 segmented and fate-colored *P. mammillata* embryos. Anterior is to the top. Color code as in Movie 1.

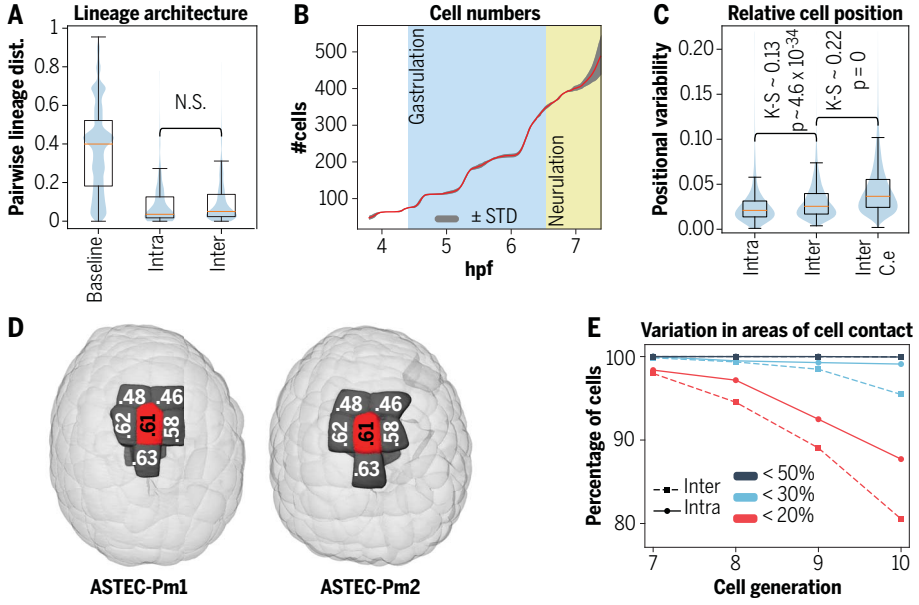

Fig. 2. Cellular reproducibility of ascidian development. (**A**) Distributions of pairwise distances between *Phallusia* cell lineage trees originated from individual cells at the 64-cell stage. Baseline: all trees; Intra: trees originating from matching bilateral left and right cells within each embryo; Inter: trees originating from homologous cells between embryos. In (A) and (C), boxes show the first, second, and third quartiles; whiskers show the range to 1.5 interquartile. N.S., not significant according to the Kolmogorov-Smirnov (K-S) test. (**B**) Comparison of the cell numbers across time between 10 individual *Phallusia* embryos after linear temporal rescaling (see supplementary materials). hpf, hours post fertilization at a temperature of 18°C. (**C**) Violin plots showing the distributions of the differences in relative cell position between matching bilateral cells in a *Phallusia* embryo (Intra), homologous *Phallusia* (Inter), or *C. elegans* (Inter C.e.) cells across embryos. (**D**) Conserved neighborhood and spatial position of the a9.61 cell in the ASTEC-Pm1 (tp73) and ASTEC-Pm2 (tp53) embryos. Ventral view. (**E**) Evolution in time (for cellular generations 7 to 10) of the percentage of cells showing a variability in areas of contact to shared neighbors smaller than the indicated thresholds between left and right cells of the same embryo (solid lines) or between homologous cells of distinct embryos (dashed lines).

To assess the developmental impact of the high genetic diversity found in ascidians (*24*), we compared the variability observed between matching bilateral cells within an embryo, which share the same genotype, with that observed between homologous cells of embryos generated from different wild-caught adults of different genotypes. Variability in cell lineage trees (Fig. 2A) and relative cell volumes (fig. S25C) of homologous cells was not significantly different within and between embryos, whereas relative cell positions (Fig. 2C) and areas of cell contacts (Fig. 2E) were only slightly less reproducible between embryos. Consistent with a developmental control, as proposed in *C. elegans* (*23*), cell position variability differed between cell lineages (fig. S27).

Areas of cell contacts are modulated by asymmetric cell divisions

Cell contact areas are determined by cell growth, cell death, cell neighbor exchanges, cell shape changes, and the geometry of cell divisions. The first three processes are absent or rare in ascidian embryos. In this study, we focused on the impact of cell divisions on cell contacts.

We first classified cell divisions into symmetric and asymmetric divisions. Symmetric divisions are defined as giving rise to two daughters with the same larval tissue fate. By contrast, asymmetric divisions produce two daughter cells differing in their larval tissue fates. Because 64-cell–stage progenitors seeding similar lineage trees, according to the tree-edit distance, adopt the same larval tissue fate (figs. S28 and S29), we identified asymmetric divisions by comparing the lineages seeded by sister cells, as exemplified in Fig. 3B. This approach correctly classified 82 and 100% of a ground truth of 28 asymmetric and 30 symmetric divisions, respectively (tables S4 to S6). The same classification, applied to cell divisions of previously undetermined status, identified 12 novel asymmetric cell divisions (table S6). These divisions were found in the lineages of larval tissues made of a diversity of cell fates or giving rise to several juvenile mesodermal and endodermal tissues. More than 32% of divisions (44 out of 136) occurring during the period considered are therefore asymmetric.

Asymmetric cell divisions have been associated to the control of cell division geometry (*25*). Most *Phallusia* embryonic cell divisions until the neurula stages produced daughters of equal volumes (fig. S30A and tables S7 and S8) and equal lifespan (fig. S30B and tables S9 and S10). Thirty-two divisions (19%), mostly found in the mesendodermal and neural lineages, produced daughters with consistently unequal volumes across embryos (Fig. 3A and tables S7 and S8). These unequal divisions also affected the timing of division of daughter cells. The larger sibling generally divided earlier (fig. S30C), in agreement with a negative

correlation between cell volume and cell cycle duration observed throughout ascidian embryogenesis (fig. S30D), as in *C. elegans* (*26*).

Inequality and asymmetry of divisions were often associated in *Phallusia*. Seventy-three percent of asymmetric cell divisions gave rise to sister cells that showed inequality in their volumes or cell cycle durations (Fig. 3C and tables S7 to S10). Conversely, 78% of geometrically unequal divisions and 92% of divisions producing sisters with asynchronous cell cycles were asymmetric (Fig. 3C and tables S6 to S10). The mid-gastrula neural plate exemplifies a near-perfect association between asymmetric divisions, geometrically unequal divisions, and asynchronously dividing sister cells (Fig. 3, D to F).

Asymmetric divisions were also preferentially associated with oriented cell divisions. By default, cells divide at 90° from the division orientation of their mother (*27*), such that a doublet of sister cells divides to form a square or tetrahedral clone of four cells (fig. S31A). We could score the orientation of 14 known symmetric, 11 known asymmetric, and 6 candidate asymmetric cell divisions. Whereas all known symmetric divisions followed the default orientation pathway, eight known and five candidate asymmetric divisions deviated from it (fig. S31, B and C).

Asymmetric cell divisions in *Phallusia* are thus associated with an active control of the volumes or relative positions of sister cells and thereby of the contact areas they establish with their neighbors. This geometrical control may be important for the differential fate specification of sister cells.

A model of geometric control of cell inductions

In ascidian embryos, most asymmetric divisions involve cell communication. Two nonexclusive mechanisms have been described. First, sister cells can be differentially induced after the division as a result of their exposure to distinct signals. Second, the mother cell can be polarized by extracellular signals before its division, causing the inheritance of activated signaling pathway components by only one of its daughters (*11*). Neural induction at the 32-cell stage involves sister differential cell induction and is controlled by the area of contact established with inducing cells (*12*), providing a proof of principle of a functional connection between cell arrangements and fate specification. To test the generality of this mechanism, we augmented our geometric description of embryogenesis with a representation of the spatiotemporal distribution of signaling pathway components (Fig. 4, A and B) and developed a theoretical framework to analyze the impact of the range of signaling proteins on inductive processes.

Given the conservation of the expression of signaling genes between *Phallusia* and *Ciona* (*28*, *29*), we inferred the expression of *Phallusia* signaling genes with cellular resolution from extensive *Ciona* signaling gene expression atlases (*30*). We focused our attention on six developmental signaling pathways (FGF, ephrin, Wnt, Bmp, Nodal, and Notch) showing patterned expression of extracellular ligands or antagonists up to the early gastrula stages (fig. S32). These pathways were sufficient to explain all known inductions up to this stage (*11*).

We next introduced a series of simplifying assumptions relative to both the competence of cells and the availability of inducing extracellular ligands. Receptors and intracellular components of the six candidate pathways were maternally expressed and their mRNAs uniformly distributed throughout the egg cytoplasm (*30*). We therefore estimated that, up to the gastrula stages, all cells were equally competent to respond to all pathways and that the receptors were uniformly distributed on cell surfaces. Extracellular ligand availability was therefore the main driver of pathway activation. When ligands and antagonists were colocalized at a cell-cell interface, secreted antagonists were assumed to fully inactivate their cognate ligands (Fig. 4D and fig. S33). Finally, we tested two scenarios for the range of secreted ligands and antagonists (Fig. 4, C and D, blue and red, respectively). This range was either limited to first-order neighbors contacting emitting cells (Fig. 4C, left) or extended to second-order neighbors (Fig. 4C, right). In both cases, potential concentration gradients were neglected, free ligands being either absent or present at a uniform concentration at the interface between two cells.

Interactions between ligands, receptors, and intracellular effectors were then modeled using the law of mass action (see supplementary materials). The cell geometry was introduced into the equations by proportionally linking the total number of receptors that could be activated by a ligand with the area of the cell exposed to free ligand molecules (Fig. 4D). For each pathway, we modeled differential sister inductions by computing the fraction of activated intracellular effectors as a function of the surface of each sister cell exposed to the inducer (Fig. 4E). In the case of polarization of the mother cell, activated effectors in each sister cell were computed from the portion of the exposed mother's surface inherited by the cell under consideration. The fraction of activated

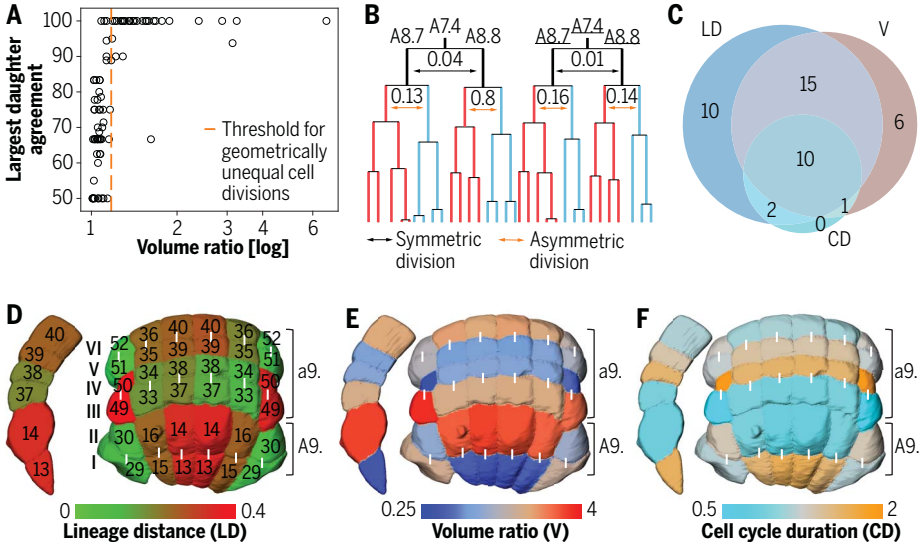

Fig. 3. Relationships between unequal cleavage, unequal cell cycle duration, and asymmetric divisions. (**A**) Unequal cell divisions between the 32-cell and neurula stages were identified as divisions in which the largest daughter is the same across >90% of all instances of this division in the dataset. (**B**) Example of symmetric and asymmetric divisions in the A7.4 neural progenitors lineages in ASTEC-Pm1 (by convention, right cells are underlined, left ones are not). The numbers indicate the tree-edit distance between the lineage trees seeded from the daughters of A8.7 and A8.8 cells. The divisions of A7.4 (right and left) are symmetric (lineage distance < 0.051), while those of A8.7 and A8.8 on both sides of the embryo are asymmetric (lineage distance > 0.051). Note the similarity of the lineages originating from the left and right A7.4 progenitors, slight division heterochronies accounting for differences in the final cell number. (**C**) Venn diagram showing the overlap of cell divisions leading to asymmetric divisions (LD), unequal sister cell cycle duration (CD), and geometrically unequal divisions (V). (**D** to **F**) Dorsal and lateral view of the a- and A-line derived neural plate, color-coded for lineage tree distance (D), volume ratios (E), and cell cycle duration ratios (F) between sister cells, linked by a white bar. The cell names are indicated in (D). Lineage tree distances are features of a cell pair, and ratios are features of individual cells.

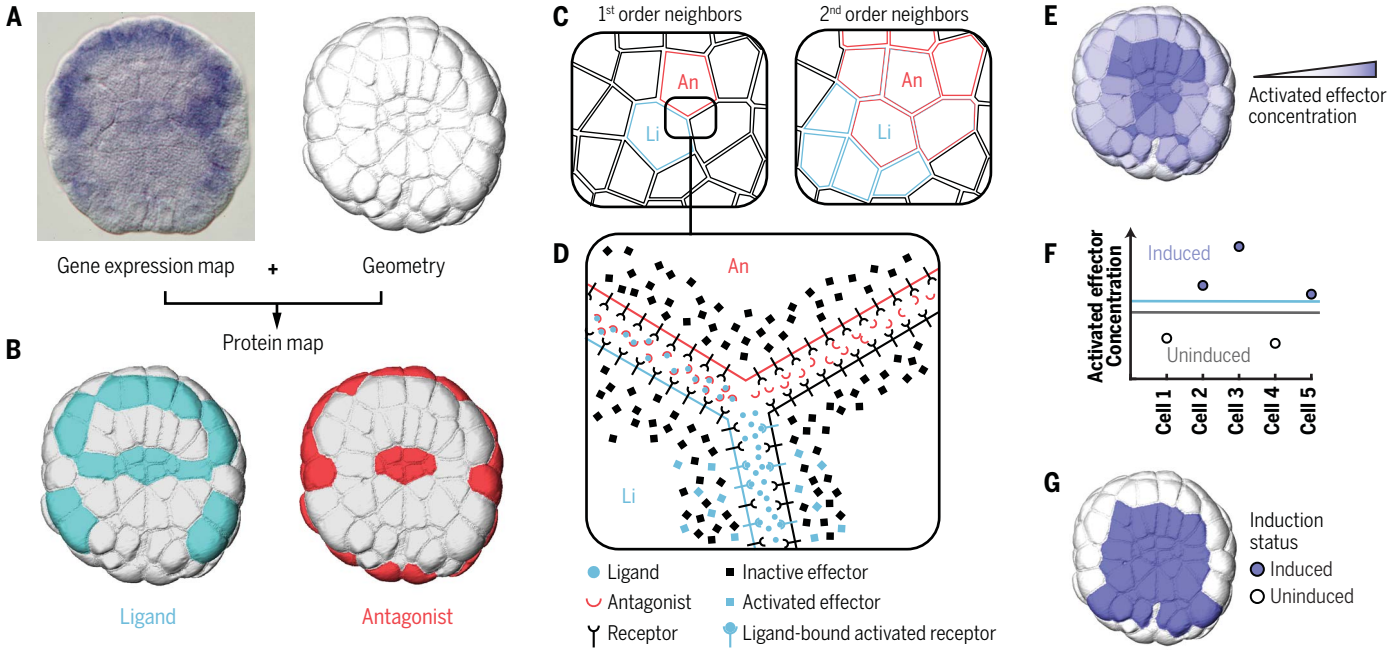

Fig. 4. Differential sister cell induction model. (**A** and **B**) Integration of gene expression information by in situ hybridization from the ANISEED database [(A), left] and geometrical information from ASTEC segmentation [(A), right] generated a map of cells expressing extracellular ligands and antagonists for the pathways of interest (B). (**C**) Schematic representation of the distribution of extracellular ligands (blue) and antagonists (red) in the vicinity of ligand-expressing (Li) or antagonist-expressing (An) cells, according to the diffusion range of proteins. (**D**) Illustration of the localization of ligands, antagonists, free or ligand-bound receptors, and active or inactive effectors at the interface of three cells expressing a ligand Li (blue cell) or its antagonist An (red cell). (**E**) Activated effector concentration map computed from the mass action law. (**F**) Theoretical schema illustrating the identification of biologically motivated induction thresholds (horizontal lines) for activated effector concentrations (see supplementary materials). (**G**) Induced cell map obtained by combining activated effector concentrations shown in (E) and activated effector concentration thresholds computed according to the principle shown in (F).

intracellular effectors is well approximated by a linearly increasing function of the area of exposure to free ligands when the areas of cell contact and the biochemical parameters remain within the range found in the literature (fig. S34).

Finally, to convert continuous levels of effector activation into a binary map of induced and uninduced cells (Fig. 4, F and G, and figs. S35 and S36), we implemented induction thresholds (Fig. 4F) governed by tunable free parameters that defined both the minimum effector activity levels for an induction and a minimum ratio of activity between induced and uninduced sister cells. This simplified differential induction model thus provides both a semi-quantitative estimate of the relative level of signaling for each pathway in each cell and a qualitative prediction of differential inductions.

Contact area–dependent inductions drive ascidian fate specification

We next explored the parameter space to adjust induction thresholds and find the best fit of the model to a ground truth of sister cells known to be differentially induced (14) or not (49). When the range of secreted protein was limited to first-order neighbors, the model, run on ASTEC-Pm1, successfully recapitulated all 14 known differential induction events with their correct inducers, with only 11 false predictions (Fig. 5A; figs. S37, and S40 to S57; and table S13). This fit was reached with a relatively large set of possible combinations of parameters values (fig. S58), which were consistent with the scientific literature [e.g., time necessary for an induction was consistent with the one found for FGF in (*31*)] (table S12). In agreement with the high rate of molecular evolution in ascidians, the affinity and concentration of ligands and receptors appeared least constrained (fig. S58). Training the model on two other embryos revealed that the predictions were robust to natural variability (figs. S38 and S39) and were obtained with similar optimal parameter sets (tables S12 and S13). The quality of the predictions, however, strongly decreased when the model was trained either without taking into account cell contact areas (Fig. 5A) or with surfaces approximated from a Voronoi tessellation of the cell barycenters (table S13). Retraining the model with a range of action of secreted ligands and inhibitors increased to second-order neighbors degraded its performance (Fig. 5A) and strongly decreased its robustness to parameter variations (fig. S58), which is consistent with the notion that secreted proteins act by direct contact to emitting cells.

The model run with short-range inducers also correctly predicted events it was not trained on. For instance, the model trained to predict differential sister induction also predicted the simultaneous induction by FGF of both daughters of the A6.1 and B6.1 endoderm precursors (*11*) (figs. S40 and S41). Running the model with optimal parameters for the wild-type (WT) situation but after virtual inactivation of ephrin receptor (Eph) signaling phenocopied the morphant Eph phenotype (*11*) and affected all FGF-mediated differential inductions except that of the daughters of the B6.4 mesenchyme and muscle precursor (*32*) (fig. S59).

Finally, we compared semiquantitative predictions of pathway activation with in vivo measurements in live embryos. We focused on the Eph-FGF/extracellular signal–regulated kinase (ERK) pathway, the main inducing pathway in early ascidian embryos (table S11) and imaged a live ERK activity biosensor, ERK–kinase translocation reporter (KTR) (*33*) (fig. S60). Experimentally measured values of ERK activity were highly reproducible between embryos (figs. S61 and S62), depended on MEK kinase activity (fig. S63), and were highly correlated to in silico predicted FGF/ERK pathway activation levels (Spearman correlation: 0.9) (Fig. 5B). Our simplified contact area–dependent induction model thus provides both reliable qualitative predictions of inductions and quantitative estimates of pathway activation levels in the different cells of WT embryos.

Robustness of ascidian fate specification to in vivo and in silico perturbations

To further analyze the sensitivity of fate specification to changes in surface of exposure to free ligand, we experimentally modified cell arrangements. Figure 5, B to D, and fig. S64 illustrate the case of a half embryo obtained by bisecting an embryo at the two-cell stage along its plane of cleavage. As expected (*12*), ectopic neural induction of epidermal precursors was observed at the 32-cell stage. The area of contact established between FGF-emitting vegetal cells and the a6.6 head epidermis precursor was strongly increased, as was the resulting ERK signaling intensity in this cell, leading to neural induction (fig. S64).

Embryo halving also affected FGF-dependent mesendodermal fate decisions at the 64-cell stage (Fig. 5, B to D). In vivo ERK signaling activity was modified in several cells, with the model correctly predicting the direction of the changes (Fig. 5B). Surface changes observed in the half embryo could even alter cell fate. During normal embryogenesis, the A6.3 mother cell divides asymmetrically to produce the A7.5 endodermal progenitor and the A7.6 trunk lateral cell progenitor. A7.5 is induced by FGF signaling, whereas the induction of A7.6 is antagonized by its contact with ephrin-expressing b-line animal cells (Fig. 5C, left: contact between the green A7.6 and the dark blue b7.9 cell) (*11*). In the half embryo, the repositioning of the B-line vegetal blastomeres sheltered A7.6 from ephrin signaling (Fig. 5C, right: contact between the green A7.6 and the ephrin-negative light blue B7.5 and B7.7 cells). As a result, A7.6 received a level of ERK signaling comparable to the induced A7.1, A7.2, A7.5, and B7.1 endodermal precursors in the half embryo and accordingly seeded an endoderm-like lineage tree (Fig. 5D and fig. S65).

Finally, we explored in silico the effect of systematic geometrical perturbations that cannot easily be generated experimentally. We ran the model with an optimal set of parameters for the WT situation but applied ±30% variation in the surface of contact to FGF-expressing cells during the 64-cell stage, without change in the contacts to ephrin-expressing cells or in the total surface of each cell. These conditions altered the predicted induction status of 8 of 32 bilateral cell pairs (Fig. 6A). Extending this approach to all pathways, 22 of 32 cell pairs changed induction status for at least one pathway upon a ±30% variation in the surface of contacts they established with signaling cells (Fig. 6A). Similar conclusions were drawn at the 112-cell stage (fig. S66). A high level of precision and reproducibility of cell-cell contacts is thus crucial for early ascidian fate specification.

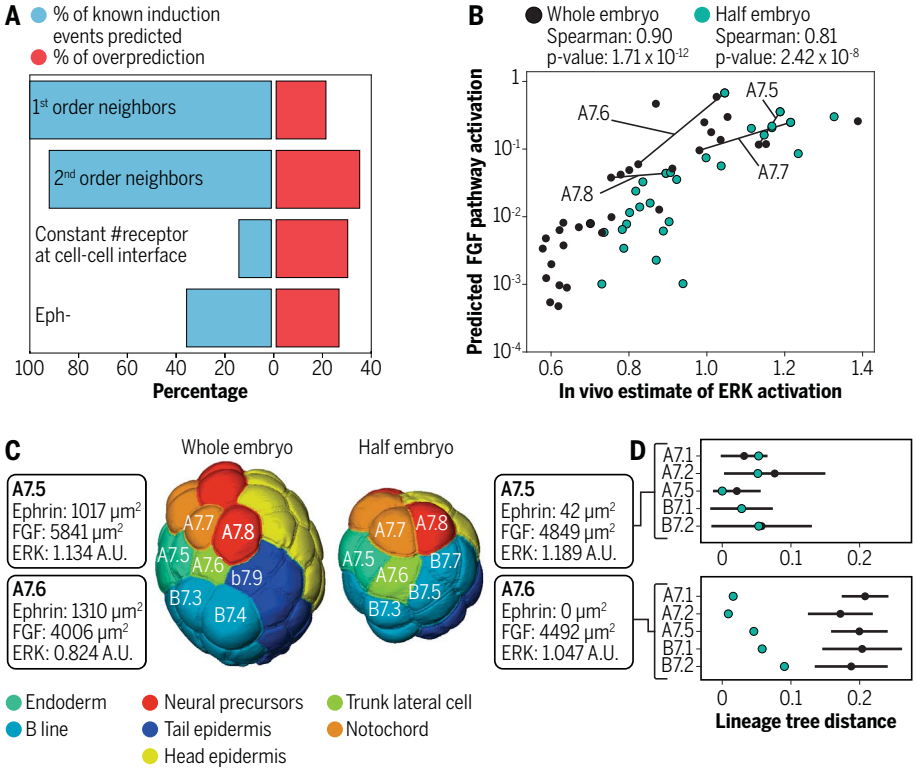

Fig. 5. Areas of contact mediate cell-cell communication. (**A**) Percentage of known (blue) or overpredicted (red) differential cell inductions predicted by the model on ASTEC-Pm1 when the range of secreted proteins is limited to first- or second-order neighbors, when the number of receptors exposed to ligands is uncoupled from the areas of contact, or when the Eph receptor is virtually inactivated. (**B**) Comparison of predicted and in vivo estimated FGF/ERK pathway activation at the 64-cell stage for a whole embryo (ASTEC-Pm13, black dots) and a half embryo (ASTEC-half-Pm1, blue-green dots). Predicted FGF pathway activity (*y* axis, log value, dimensionless) was obtained by running the model without diffusion. In vivo ERK activation (*x* axis, [fluorescence intensity]$^{-1}$) was estimated by imaging ERK-KTR-Clover-expressing embryos and determining the normalized nuclear amount of reporter, whose inverse provides an estimate of the log value of ERK activation (see supplementary materials section 10.1.3). The Spearman's correlation coefficient (S) and *P* value that this correlation is obtained by chance are indicated for both datasets. (**C**) Lateral views of mid-64-cell stage whole and half embryos with indication of cell fates, cell names, cell neighborhood, and areas of contact to FGF- and ephrin-expressing cells and ERK signaling activity (inverse normalized nuclear KTR values) of the A7.5 (blue-green) and A7.6 (green) cells. A.U., arbitrary units. (**D**) (Top) Distances between the lineage trees seeded by A7.5 and the indicated endodermal precursors in ASTEC-half-Pm1 (blue-green dots). Black dots indicate the average lineage distance, in whole embryos (ASTEC-Pm1 to -Pm8), of A7.5 to the indicated cells. The black line represents one standard deviation. (Bottom) Same analysis, but for the trunk lateral cell precursor A7.6 [green in (C)]. Embryo halving does not substantially affect the lineage distance of A7.5 to endoderm but shifts the lineage seeded by A7.6 to an endoderm-like one.

Concluding remarks

In this work, we systematically quantified and analyzed the behavior and fate decisions of individual embryonic cells across gastrulation and neurulation in *Phallusia*. We then enriched this geometric description with measurements of signaling activities and gene expression activity. Combined with high throughput single-cell genomics data (*34*), emerging computational methods to map such data onto reference geometrical descriptions (*35*), and the determination of mechanical properties by inference from the geometry or by direct force measurements (*36*, *37*), our work establishes the ascidian embryo as a system to bridge cell behaviors, the forces that drive morphogenesis, and the underlying regulatory program.

Descriptions of cell inductions during animal embryogenesis often highlight the role of long-range morphogen gradients (*38*). In this scenario, the outcome of a cell communication event is determined by local morphogen concentrations, whereas variations in individual cell contacts are considered to play a minor part (Fig. 6B, top). Here, we show that areas of contact between communicating cells have a sufficient encoding potential to explain most fate specification events in a chordate embryo (Fig. 6B, bottom), extending previous work in ascidians and vertebrates (*12*, *39*). Our work thus reveals that quantitative cues can shift from ligand concentration

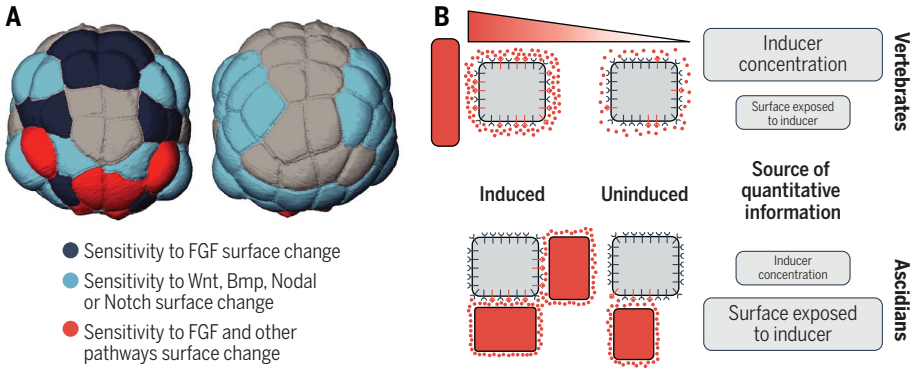

Fig. 6. Contact area–dependent cell inductions constrain embryonic geometries. (**A**) Projection onto a 64-cell–stage embryo of cells whose predicted induced state changed when exposed to a ±30% in silico change in their area of contact to cells expressing FGF (dark blue), ligands or inhibitors of other pathways (light blue), or both (red). See also fig. S66 for corresponding data at the 112-cell stage. (**B**) Comparison of two modes of cell induction: diffusible morphogen gradients, as proposed for vertebrates, and contact area–dependent cell inductions, as proposed for ascidians. In the former, secreted inducer concentration is the major determinant of induction; in the latter, the area exposed to the ligand plays a major role.

to areas of cell contacts. Consistent with an equivalence of processes, variations in cell contact areas or in ligand concentrations have comparable effects on ascidian cell inductions (fig. S67).

The prevalent use of contact area–dependent inductions may also causally explain the counterintuitive association between the cellular reproducibility of the ascidian embryonic program and a high level of genetic divergence. Precisely and robustly shaping a morphogen gradient involves the coordinated recruitment of multiple cellular functions to control the production, degradation, transport, or endocytosis of ligands and receptors (*38*). Because of the shallowness and noisiness of such gradients, additional layers of regulatory cross-talk between target transcription factors (*38*) or subsequent cell sorting (*40*) are needed to transform the coarse information provided by the gradient into sharp boundaries. The precise response to long-range morphogen gradients thus involves sophisticated layers of regulation, which may constrain the architecture of regulatory networks and global genome evolution. By contrast, the surface-of-contact–dependent signaling we described here ensures that sister cells are exposed to sufficiently different signals to directly define boundaries, thereby limiting the need for subsequent transcriptional refinements. Contact area–dependent inductions are therefore likely to involve fewer layers of regulation than long-range morphogen gradients, thereby relaxing constraints on genome evolution.

Methods summary

All methods used in this study are recapitulated in detail in the supplementary materials, which include the following 14 sections: (i) the imaging protocol, (ii) the preprocessing of the movies of *P. mammillata* development, (iii) the limitation of the state-of-the art methods for cell segmentation and tracking, (iv and v) our segmentation and tracking algorithm (ASTEC) and its postprocessing step, (vi) the quantification of the quality of the segmentations and trackings, (vii and viii) the analysis of developmental stereotypy and fate restriction events, (ix) the mathematical model of cell-cell signaling, (x) the validation of the model through the in vivo measurement of ERK signaling, and (xi) the validation of the model through the analysis of the effect of experimental perturbations of surfaces of contacts. Sections xii to xiv describe the authors' contributions, list the tables, and indicate how to access software and datasets.

Note added in proof: A reference (*106*) was added at proof stage to a relevant new resource on single-cell transcriptional profiles covering *P. mammillata* early embryogenesis.

REFERENCES AND NOTES

1. A. Pierre, J. Sallé, M. Wühr, N. Minc, Generic theoretical models to predict division patterns of cleaving embryos. *Dev. Cell* **39**, 667–682 (2016). doi: 10.1016/j.devcel.2016.11.018; pmid: 27997824
2. J. E. Sulston, E. Schierenberg, J. G. White, J. N. Thomson, The embryonic cell lineage of the nematode *Caenorhabditis elegans*. *Dev. Biol.* **100**, 64–119 (1983). doi: 10.1016/0012-1606(83)90201-4; pmid: 6684600
3. P. Lemaire, Evolutionary crossroads in developmental biology: The tunicates. *Development* **138**, 2143–2152 (2011). doi: 10.1242/dev.048975; pmid: 21558365
4. F. Delsuc, H. Brinkmann, D. Chourrout, H. Philippe, Tunicates and not cephalochordates are the closest living relatives of vertebrates. *Nature* **439**, 965–968 (2006). doi: 10.1038/nature04336; pmid: 16495997
5. B. Goldstein, On the evolution of early development in the Nematoda. *Philos. Trans. R. Soc. London Ser. B* **356**, 1521–1531 (2001). doi: 10.1098/rstb.2001.0977; pmid: 11604120
6. F. Delsuc *et al.*, A phylogenomic framework and timescale for comparative studies of tunicates. *BMC Biol.* **16**, 39 (2018). doi: 10.1186/s12915-018-0499-2; pmid: 29653534
7. A. Stolfi *et al.*, Divergent mechanisms regulate conserved cardiopharyngeal development and gene expression in distantly related ascidians. *eLife* **3**, e03728 (2014). doi: 10.7554/eLife.03728; pmid: 25209999
8. H. Nishida, Cell lineage analysis in ascidian embryos by intracellular injection of a tracer enzyme. III. Up to the tissue restricted stage. *Dev. Biol.* **121**, 526–541 (1987). doi: 10.1016/0012-1606(87)90188-6; pmid: 3582738
9. D. A. Voronov, Y. V. Panchin, Cell lineage in marine nematode *Enoplus brevis*. *Development* **125**, 143–150 (1998). pmid: 9389672
10. H. Nishida, Specification of embryonic axis and mosaic development in ascidians. *Dev. Dyn.* **233**, 1177–1193 (2005). doi: 10.1002/dvdy.20469; pmid: 15973692
11. P. Lemaire, Unfolding a chordate developmental program, one cell at a time: Invariant cell lineages, short-range inductions and evolutionary plasticity in ascidians. *Dev. Biol.* **332**, 48–60 (2009). doi: 10.1016/j.ydbio.2009.05.540; pmid: 19433085
12. O. Tassy, F. Daian, C. Hudson, V. Bertrand, P. Lemaire, A quantitative approach to the study of cell shapes and interactions during early chordate embryogenesis. *Curr. Biol.* **16**, 345–358 (2006). doi: 10.1016/j.cub.2005.12.044; pmid: 16488868
13. G. de Medeiros *et al.*, Confocal multiview light-sheet microscopy. *Nat. Commun.* **6**, 8881 (2015). doi: 10.1038/ncomms9881; pmid: 26602977
14. V. Ulman *et al.*, An objective comparison of cell-tracking algorithms. *Nat. Methods* **14**, 1141–1152 (2017). doi: 10.1038/nmeth.4473; pmid: 29083403
15. E. Faure *et al.*, A workflow to process 3D+time microscopy images of developing organisms and reconstruct their cell lineage. *Nat. Commun.* **7**, 8674 (2016). doi: 10.1038/ncomms9674; pmid: 26912388
16. J. Stegmaier *et al.*, Real-time three-dimensional cell segmentation in large-scale microscopy data of developing embryos. *Dev. Cell* **36**, 225–240 (2016). doi: 10.1016/j.devcel.2015.12.028; pmid: 26812020
17. Y. Azuma, S. Onami, Biologically constrained optimization based cell membrane segmentation in *C. elegans* embryos. *BMC Bioinformatics* **18**, 307 (2017). doi: 10.1186/s12859-017-1717-6; pmid: 28629355
18. P. Villoutreix *et al.*, An integrated modelling framework from cells to organism based on a cohort of digital embryos. *Sci. Rep.* **6**, 37438 (2016). doi: 10.1038/srep37438; pmid: 27910875
19. M. A. Luengo-Oroz *et al.*, *3D+t* morphological processing: Applications to embryogenesis image analysis. *IEEE Trans. Image Process.* **21**, 3518–3530 (2012). doi: 10.1109/TIP.2012.2197007; pmid: 22562755
20. R. Fernandez *et al.*, Imaging plant growth in 4D: Robust tissue reconstruction and lineaging at cell resolution. *Nat. Methods* **7**, 547–553 (2010). doi: 10.1038/nmeth.1472; pmid: 20543845
21. B. Leggio *et al.*, *MorphoNet*: An interactive online morphological browser to explore complex multi-scale data. *Nat. Commun.* **10**, 2812 (2019). doi: 10.1038/s41467-019-10668-1; pmid: 31249294
22. W. R. Jeffery, Programmed cell death in the ascidian embryo: Modulation by FoxA5 and Manx and roles in the evolution of larval development. *Mech. Dev.* **118**, 111–124 (2002). doi: 10.1016/S0925-4773(02)00236-8; pmid: 12351175
23. X. Li *et al.*, Systems properties and spatiotemporal regulation of cell position variability during embryogenesis. *Cell Rep.* **26**, 313–321.e7 (2019). doi: 10.1016/j.celrep.2018.12.052; pmid: 30625313
24. E. M. Leffler *et al.*, Revisiting an old riddle: What determines genetic diversity levels within species? *PLOS Biol.* **10**, e1001388 (2012). doi: 10.1371/journal.pbio.1001388; pmid: 22984349
25. X. Morin, Y. Bellaïche, Mitotic spindle orientation in asymmetric and symmetric cell divisions during animal development. *Dev. Cell* **21**, 102–119 (2011). doi: 10.1016/j.devcel.2011.06.012; pmid: 21763612
26. Y. Arata, H. Takagi, Y. Sako, H. Sawa, Power law relationship between cell cycle duration and cell volume in the early embryonic development of *Caenorhabditis elegans*. *Front. Physiol.* **5**, 529 (2015). doi: 10.3389/fphys.2014.00529; pmid: 25674063
27. S. Strome, Determination of cleavage planes. *Cell* **72**, 3–6 (1993). doi: 10.1016/0092-8674(93)90041-N; pmid: 8422680
28. A. Madgwick *et al.*, Evolution of embryonic *cis*-regulatory landscapes between divergent *Phallusia* and *Ciona* ascidians. *Dev. Biol.* **448**, 71–87 (2019). doi: 10.1016/j.ydbio.2019.01.003; pmid: 30661644
29. U.-M. Fiuza, T. Negishi, A. Rouan, H. Yasuo, P. Lemaire, A Nodal/Eph signalling relay drives the transition from apical constriction to apico-basal shortening in ascidian endoderm

invagination. bioRxiv 418988 [Preprint]. 1 December 2019. https://doi.org/10.1101/418988.
30. J. Dardaillon *et al*., ANISEED 2019: 4D exploration of genetic data for an extended range of tunicates. *Nucleic Acids Res.* **48**, D668–D675 (2019). doi: 10.1093/nar/gkz955; pmid: 31680137
31. G. J. Kim, A. Yamada, H. Nishida, An FGF signal from endoderm and localized factors in the posterior-vegetal egg cytoplasm pattern the mesodermal tissues in the ascidian embryo. *Development* **127**, 2853–2862 (2000). pmid: 10851130
32. G. J. Kim, G. Kumano, H. Nishida, Cell fate polarization in ascidian mesenchyme/muscle precursors by directed FGF signaling and role for an additional ectodermal FGF antagonizing signal in notochord/nerve cord precursors. *Development* **134**, 1509–1518 (2007). doi: 10.1242/dev.02825; pmid: 17360771
33. C. de la Cova, R. Townley, S. Regot, I. Greenwald, A real-time biosensor for ERK activity reveals signaling dynamics during *C. elegans* cell fate specification. *Dev. Cell* **42**, 542–553.e4 (2017). doi: 10.1016/j.devcel.2017.07.014; pmid: 28826819
34. C. Cao *et al*., Comprehensive single-cell transcriptome lineages of a proto-vertebrate. *Nature* **571**, 349–354 (2019). doi: 10.1038/s41586-019-1385-y; pmid: 31292549
35. M. Nitzan, N. Karaiskos, N. Friedman, N. Rajewsky, Gene expression cartography. *Nature* **576**, 132–137 (2019). doi: 10.1038/s41586-019-1773-3; pmid: 31748748
36. K. Sugimura, P.-F. Lenne, F. Graner, Measuring forces and stresses in situ in living tissues. *Development* **143**, 186–196 (2016). doi: 10.1242/dev.119776; pmid: 26786209
37. K. Sherrard, F. Robin, P. Lemaire, E. Munro, Sequential activation of apical and basolateral contractility drives ascidian endoderm invagination. *Curr. Biol.* **20**, 1499–1510 (2010). doi: 10.1016/j.cub.2010.06.075; pmid: 20691592
38. A. Sagner, J. Briscoe, Morphogen interpretation: Concentration, time, competence, and signaling dynamics. *WIREs Dev. Biol.* **6**, e271 (2017). doi: 10.1002/wdev.271; pmid: 28319331
39. O. Shaya *et al*., Cell-cell contact area affects notch signaling and notch-dependent patterning. *Dev. Cell* **40**, 505–511.e6 (2017). doi: 10.1016/j.devcel.2017.02.009; pmid: 28292428
40. F. Xiong *et al*., Specified neural progenitors sort to form sharp domains after noisy Shh signaling. *Cell* **153**, 550–561 (2013). doi: 10.1016/j.cell.2013.03.023; pmid: 23622240

ACKNOWLEDGMENTS

We thank the members of the Lemaire, Godin, and Hufnagel teams for discussion and advice throughout this project; P. Kristofori (CRBM) for contributions to the analysis of KTR experiments; T. Rasse (EMBL) for running RACE on ascidian datasets; J. Stegmaier (RWTH Aachen University, Germany) for advice; A. McDougall (LBDV, Villefranche/mer, France) for the generous gift of the PH-GFP expression construct; and Y. Hitoyoshi (LBDV, Villefranche/mer, France) for the PH-Tdtomato expression construct. We thank T. Schneidt (EMBL) for help with building the pGEM-PH-citrine construct and P. Neveu (EMBL) for discussions on cloning methods. We thank the Montpellier Image Resources (MRI) facility for hosting the MuViSPIM used in this study and S. de Rossi (MRI) for providing expert help with the MuViSPIM. We are grateful to P.-J. Keller and A. Pavlopoulos (Janelia Research Labs, USA), to F. Fagotto (CRBM, Montpellier, France), and to P. Ônal (NYU) for critical reading of the manuscript. We also thank the Montpellier SI2C2 service for IT support and P. Richard and M. Plays (CRBM) for careful animal husbandry. **Funding:** This work was funded by core support from CNRS to P.L.; by Inria (core support and IPL Morphogenetics) to C.G. and G.Ma.; by the Geneshape project (ANR-SYSC-018-02) to P.L. and C.G.; and by the Dig-Em project (ANR-14-CE11-0013-01) to P.L., C.G., and G.Ma. L.H. was supported by the European Molecular Biology Laboratory and the Center of Modeling and Simulation in the Biosciences (BIOMS) of the University of Heidelberg. L.G. was supported by a doctoral contract from the CBS2 doctoral school of the University of Montpellier 2, by the Fondation pour la Recherche Médicale (FRM) (FDT20140931061), and by the Morphoscope2 Equipex project (ANR-11-EQPX-0029). U.-M.F. was supported by the Geneshape and Dig-Em projects, by the FRM (SPF20120523969), and by the EMBL Interdisciplinary Postdoc Programme under Marie Curie Actions. The Institut de Biologie Computationnelle of Montpellier (IBC; ANR-11-BINF-0002) supported E.F. and B.L. B.L. and J.L. were supported by the Dig-Em project. G.Mi. was supported by Inria (IPL Morphogenetics) and the Dig-Em project. K.B. was supported by a Ph.D. contract from the EpiGenMed laboratory of excellence (ANR-10-LABX-12-01). The Fondation Bettencourt-Schueller funded the Montpellier MuViSPIM (with a contribution from the University of Montpellier). **Author contributions:** Author contributions are listed in detail in the supplementary materials. **Data and materials availability:** See supplementary materials. The software, standard parameter files, and tutorials have been deposited to Github (https://github.com/astec-segmentation). All digitized embryos (fused intensity movies, segmentations, and meshes) have been deposited to figshare (https://figshare.com/projects/Phallusia_mammillata_embryonic_development/64301) and can be interactively explored through MorphoNet (www.morphonet.org/). All instructions and links are detailed and kept up to date in the ASTEC webpage of our institute (www.crbm.cnrs.fr/en/astec/).

SUPPLEMENTARY MATERIALS

science.sciencemag.org/content/369/6500/eaar5663/suppl/DC1
Materials and Methods
Supplementary Text
Figs. S1 to S67
Tables S1 to S13
References (*41*–*106*)
MDAR Reproducibility Checklist
Data S1 to S18
Movies S1 to S4

View/request a protocol for this paper from *Bio-protocol*.

4 December 2019; accepted 29 April 2020
10.1126/science.aar5663

Contact area–dependent cell communication and the morphological invariance of ascidian embryogenesis

Léo Guignard, Ulla-Maj Fiúza, Bruno Leggio, Julien Laussu, Emmanuel Faure, Gaël Michelin, Kilian Biasuz, Lars Hufnagel, Grégoire Malandain, Christophe Godin and Patrick Lemaire

Science **369** (6500), eaar5663.
DOI: 10.1126/science.aar5663

Cell-cell contacts specify cell fate

Ascidians, or sea squirts, are marine invertebrate filter feeders with highly reproducible cellular events and invariant embryonic cell lineages. Guignard *et al.* studied the ascidian embryo to address the determinants of this cellular reproducibility. They introduce computational methods for the robust and automated segmentation, tracking, and analysis of whole-cell behaviors in high-throughput light-sheet microscopy datasets. This work shows that cell induction can be controlled by the contact area among cells. The range of cell signaling is proposed to set the scale at which animal embryonic reproducibility is observed. A high level of reproducibility of embryonic geometries may also counter-intuitively lift constraints on genome evolution, thereby contributing to the rapid molecular evolution observed in ascidians.

Science, this issue p. eaar5663